Radiation Physics and Chemistry 166 (2020) 108488

Contents lists available at ScienceDirect

Radiation Physics and Chemistry

journal homepage: www.elsevier.com/locate/radphyschem

Suborgan breast dosimetry for breast nuclear medicine imaging using anthropomorphic software breast phantoms

Yan-Lin Liu[a], Shu-Jun Chang[b], Fang-Yi Lin[a], Tien-Yu Chang[c], Jay Wu[a,*]

[a] Department of Biomedical Imaging and Radiological Sciences, National Yang-Ming University, Taipei, Taiwan
[b] Health Physics Division, Institute of Nuclear Energy Research, Atomic Energy Council, Taoyuan, Taiwan
[c] Department of Radiology, Cheng Hsin General Hospital, Taipei, Taiwan

ARTICLE INFO

Keywords:
Breast nuclear medicine imaging
Anthropomorphic software breast phantom
S value

ABSTRACT

Breast nuclear medicine imaging has gradually become a supplemental method for detection of mammographically occult cancer in dense breasts. However, mammary glands and ducts are highly sensitive to radiation; the absorbed dose to glandular tissue may increase the risk of secondary breast cancer. Therefore, accurate suborgan breast dosimetry for breast nuclear medicine imaging represents an important issue. In this study, a series of anthropomorphic software breast phantoms (ASBPs) with various volumes and glandularities were built. The realism of the ASBPs was assessed by using the two-dimensional projection and fractal dimension (FD) analysis. Breast self S values and suborgan S values for ^{18}F and ^{99m}Tc were simulated using the Monte Carlo technique. The projected images of the ASBPs were similar to clinical mammograms in tissue distribution and image contrast. The mean FD value for the ASBPs was 2.23. The maximum differences between the breast self S values of ASBPs and OLINDA/EXM for ^{18}F and ^{99m}Tc were −14.4% and −16.7%, respectively. For the breast suborgan S values, the maximum ratios between the S value from gland to gland S(g←g) and the S value from breast to breast S(b←b) were 4.84 for ^{18}F and 3.60 for ^{99m}Tc. The mean ratios between the S value from gland to duct S(d←g) and that from gland to gland S(g←g) were 0.296 for ^{18}F and 0.356 for ^{99m}Tc. The suborgan breast dosimetry based on the ASBPs can be used for internal dose evaluation and carcinogenic risk assessment of mammary glands and ducts in breast nuclear medicine imaging.

1. Introduction

Clinical screening of breast cancer is mainly performed using X-ray mammography and supplemented by ultrasound and magnetic resonance imaging (MRI). Although mammography possesses high sensitivity and specificity for identification of microcalcifications (Hofvind et al., 2012), its performance is significantly affected by breast density. In recent years, the application of breast-specific gamma imaging (BSGI) and positron emission mammography (PEM) has markedly increased for detection of mammographically occult cancer, especially in women with dense breasts. BSGI and PEM are a kind of nuclear medicine examinations that patients receive an intravenous injection of radiopharmaceuticals and are being subsequently imaged with gamma camera or positron emission tomography (Hruska, 2017). The breast dose assessment for nuclear medicine imaging is based on the evaluation of the whole breast dose under the assumption of uniform distribution of radiopharmaceuticals in the breast. However, the most radiation-sensitive tissue in the breast is the glandular tissue (Drooger et al., 2015), where the radiopharmaceuticals accumulate. Therefore, the development of suborgan breast dosimetry for breast nuclear medicine imaging is essential.

When assessing the absorbed dose to the breast, homogeneous tissue-equivalent phantoms with various densities are frequently used (Lai et al., 2015; Sarno et al., 2017). However, the use of homogeneous phantoms may result in a 30% error margin for the absorbed dose evaluation because of the tree-like distribution of glandular tissue (Hernandez et al., 2015). For realistic breast modeling, voxel phantoms based on computed tomography (CT) scans or MRI have been constructed to investigate the mean glandular dose (MGD) for mammography (Nigapruke et al., 2010; Mohammadyari et al., 2015). Although the voxel breast phantoms are highly realistic, they are based on individual image data and cannot be used as a general dosimetry standard. Additionally, they are mainly used for external dose evaluation. Anthropomorphic software breast phantoms (ASBPs) have been built

* Corresponding author. Associate Professor Department of Biomedical Imaging and Radiological Sciences, National Yang-Ming University, No.155, Sec.2, Linong Street, Taipei, 11221, Taiwan.
E-mail address: jaywu@ym.edu.tw (J. Wu).

https://doi.org/10.1016/j.radphyschem.2019.108488
Received 8 April 2019; Received in revised form 13 July 2019; Accepted 9 September 2019
Available online 10 September 2019
0969-806X/

based on mathematical formulas (Bakic et al., 2003, 2011; Chen et al., 2011; Mahr et al., 2012). The breast contour was constructed by using semi-ellipsoids or second-degree polynomials. The adipose tissue and glandular tissue were created using the region-growing method to simulate the real tissue distribution (Bakic et al., 2011). The ASBPs have the potential to be applied to internal dose evaluation of the breast in BSGI and PEM.

In nuclear medicine dosimetry, the medical internal radiation dose (MIRD) schema is primarily used for assessing internal organ doses (Loevinger et al., 1988). In this schema, the average organ dose is the product of cumulative activity in source organ and S value from source to target organs. For tissue dose evaluation, suborgan dosimetry has been proposed for various organs, such as the heart (Coffey et al., 1981), brain (Bouchet et al., 1999), and kidney (Bouchet et al., 2003). Villoing et al. (2019) further built a series of head phantoms with detailed cranial structures to obtain the suborgan S values for nuclear medicine neuroimaging. However, for the breast dosimetry, only organ S values are available at present. In this study, the ASBPs of various volumes and glandularities were built and verified. The breast S values were simulated using the Monte Carlo technique, and the suborgan S values of mammary glands and ducts were obtained for ^{18}F and ^{99m}Tc. The purpose of this study was to propose the breast suborgan dosimetry for dose evaluation of mammary glands and ducts in BSGI and PEM.

2. Materials and methods

2.1. MIRD schema

The MIRD schema is used to assess the absorbed dose to the entire organ or tissue subregions for internal exposure (Bolch et al., 2009). The absorbed dose to the target organ or tissue r_T is defined as follows:

$$D(r_T, T_D) = \sum_{r_S} \tilde{A}(r_S, T_D) S(r_T \leftarrow r_S) \quad (1)$$

where T_D is the dose-integration period and $\tilde{A}(r_S, T_D)$ is the time-integrated activity, which is the total number of decays of the radionuclide in source organ or tissue r_S. $S(r_T \leftarrow r_S)$ is the absorbed dose of r_T caused by one transformation of the radionuclide in r_S, which is called the S value. In the generalized MIRD formula, the time-integrated activity $\tilde{A}$ is a patient-specific measure related to the metabolism and biodistribution of radiopharmaceuticals in the patient. The S value is a radionuclide-specific quantity that reflects the decay characteristics of the radionuclide and the geometric model of r_S and r_T, as follows:

$$S(r_T \leftarrow r_S) = \frac{1}{M(r_T)} \sum_i \Delta_i \phi(r_T \leftarrow r_S, E_i) \quad (2)$$

where $M(r_T)$ is the mass of r_T, Δ_i is the total energy of the ith radiation emitted from the radionuclide, and $\varphi(r_T \leftarrow r_S, E_i)$ is the absorption fraction defined as the fraction of energy E_i emitted from r_S that is absorbed in r_T. φ/M is also referred to as the specific absorbed fraction. The source tissue and target tissue we care about in BSGI and PEM is the glandular tissue; however, only the organ S values have been proposed for breast dose assessment so far. Through the following ASBP construction and Monte Carlo simulation, we can obtain the breast suborgan S values for internal dose evaluation of the breast.

2.2. Definition of volumes and regions in ASBPs

Statistical data from breast CT images indicate that the breast volume generally ranges from 400 to 1000 ml (Erickson et al., 2016). Therefore, three sizes of the ASBPs were constructed including 500, 750, and 1000 ml (Fig. 1). The fibroglandular growth region was formed by using the difference set between two ellipsoids, whereas the adipose growth region was defined as the difference set between breast contour and fibroglandular region. The *xyz* dimensions of the 500, 750, and 1000-ml ASBPs were $17.5 \times 11 \times 5$, $20 \times 13 \times 5.5$, and $21 \times 14 \times 6.5\,\text{cm}^3$, respectively. The length of each axis was randomly multiplied by 0.9–1.1. The breast contour was extended outwards by 0.2 cm to form a skin layer.

2.3. Construction of tissue structures in ASBPs

The adipose tissue in the adipose growth region was built using an iterative region-growing algorithm (Bakic et al., 2011). Arcs with different curvatures were generated from the nipple to the chest wall. Seed points were stochastically produced on the arcs, and each seed was grown concurrently into an ellipsoid with randomly sampled speed and direction. The extended area of the seed was treated as inactive if it was in contact with the skin, chest wall, other adipose ellipsoids, or fibroglandular region. The iterative process continued until the adipose growth region was filled up. The junction between the extended seeds was deemed to be Cooper's ligaments. In the fibroglandular growth region, the seed points were grown in the same way as they were grown in the adipose growth region until the glandularity, the mass ratio between glandular tissue and breast, reached 20%, 30%, 40%, and 50%. The random growth process causes the adipose tissue to produce irregular shapes that mimic the real anatomical structure of the breast (Bakic et al., 2011).

The models of mammary ducts in the ASBPs were built using the binary tree and the ramification matrix (Bakic et al., 2003). According to clinical human mammary duct anatomy (Going and Moffat, 2004; Ohtake et al., 2001), a series of elliptical cylinders with an initial length h_0 of 7 mm and a radius r_0 of 1 mm was extended from the nipple to form a tree-like structure. The length of the ith newly-generated duct was set to $h_{i-1} \times (1+\zeta) \times 0.5$, where ζ is a random number between 0 and 1 with a uniform distribution. The minimum length was 3 mm. The radius of a newly generated duct was set to $h_i \times r_0/h_0$. The initial azimuthal angle ϕ of the duct was 60°, and the azimuthal angle of subsequent ducts was randomly sampled between 0° and 360°. The initial polar angle θ of the duct was 30°, whereas the following polar angle was determined by using $\theta_{i-1} \times (\zeta + 0.5)$, where ζ is another random number between 0 and 1. A 3D model of a 500-ml ASBP with 20% glandularity is shown in Fig. 2.

2.4. Verification of ASBPs

For verification of the realism of the ASBPs, three sets of the ASBPs were generated for each volume-glandularity combination. The mean and standard deviation of breast mass, glandular mass, and glandularity were calculated. The ASBPs were projected to the mediolateral direction by using an X-ray imaging simulator (XRaySim) (Lazos et al., 2000). A tube voltage of 30 kV was applied to generate the X-ray spectrum produced by the Mo target in mammography. The corresponding linear attenuation coefficients of the skin, glandular tissue, adipose tissue, and Cooper's ligament were 0.3819, 0.3650, 0.3118, and 0.3557 cm^{-1}, respectively (Berger, 1999; Hammerstein et al., 1979). In addition to visual assessment of the projected images of the ASBPs, a region of interest (ROI) with 64×64 pixels was drawn in the central breast region. The power spectrum of the ROI was obtained using the circular-averaged power spectrum method (Tourassi et al., 2006). The fractal dimension (FD) analysis was performed with the formula $FD = (8-\beta)/2$, where β is the slope of the linear regression line of the 1-dimensional power spectrum in the log-log plot.

2.5. Monte Carlo simulation

The Monte Carlo N-Particle eXtended (MCNPX) transport code (Pelowitz et al., 2011) was used to simulate breast self S values and suborgan S values. The ASBPs were resampled to $200 \times 200 \times 200$ voxels. Each voxel was filled with corresponding tissue types, including the adipose tissue, glandular tissue, mammary duct, skin, and ligament. Non-tissue voxels were deemed to be air. The ASBP was constructed

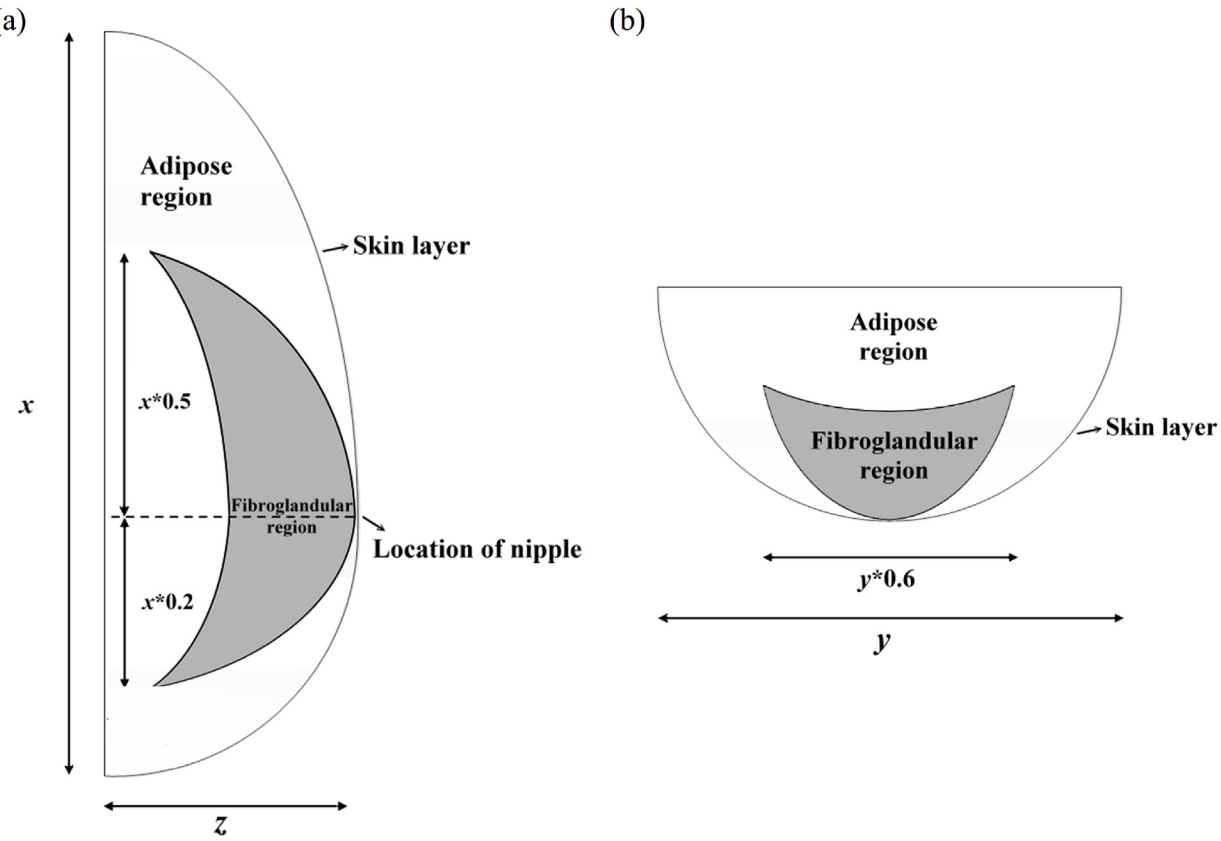

Fig. 1. (a) Sagittal and (b) transverse diagrams of the ASBPs. Areas in white and gray represent the adipose and fibroglandular growth regions. For 500, 750, and 1000-ml breast models, the *xyz* dimensions are 17.5 × 11 × 5, 20 × 13 × 5.5, and 21 × 14 × 6.5 cm^3.

using the repeated structure and lattice geometry in MCNPX. For elemental composition and density of the tissues, the data were adopted from Hammerstein et al. (1979). For radiation source terms, ^{99m}Tc was simulated for ^{99m}Tc-sestamibi used in BSGI, and ^{18}F was simulated for ^{18}F-fluorodeoxyglucose (FDG) used in PEM. The number of simulated particles for each case was fixed at 50 million to reduce the relative coefficient of variation (%CV) to less than 5%.

2.6. Simulation of S values

For cases that radioisotopes were uniformly distributed in the whole breast, the self S values from breast to breast S(b←b) for each volume-glandularity combination of the ASBPs were simulated. The results were compared with the S values calculated using the OLINDA/EXM nodule module (Stabin et al., 2005). For suborgan breast dosimetry, energy deposition in target tissue was tallied assuming a uniform distribution of radioisotopes in source tissue. Three types of suborgan S values were obtained, including breast as source tissue and gland as target tissue S(g←b), gland as both source and target tissues S(g←g), and gland as source tissue and mammary duct as target tissue S(d←g).

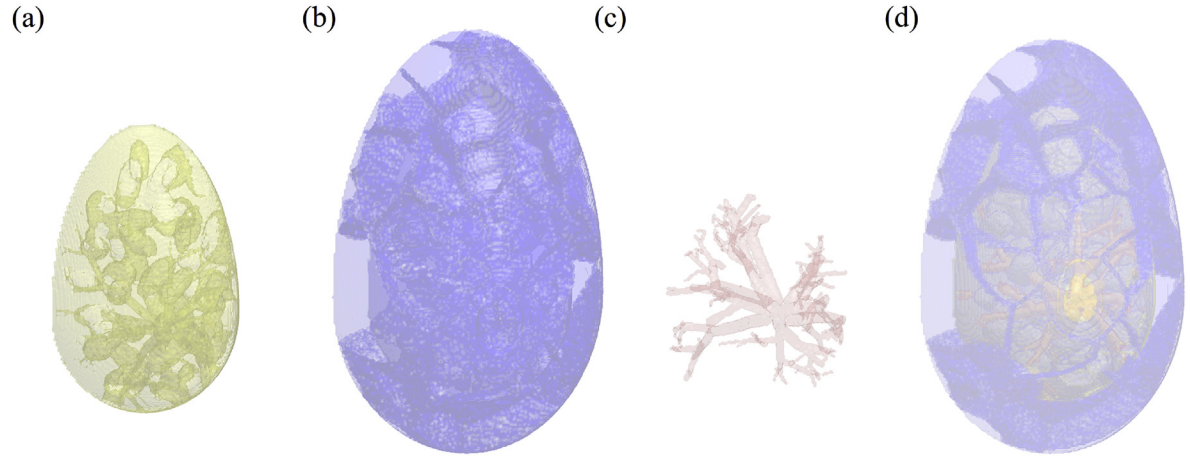

Fig. 2. 3D model of a 500-ml ASBP with 20% glandularity, including (a) the fibroglandular growth region with adipose tissue, (b) the adipose growth region with Cooper's ligaments, (c) the mammary ducts, and (d) the whole breast.

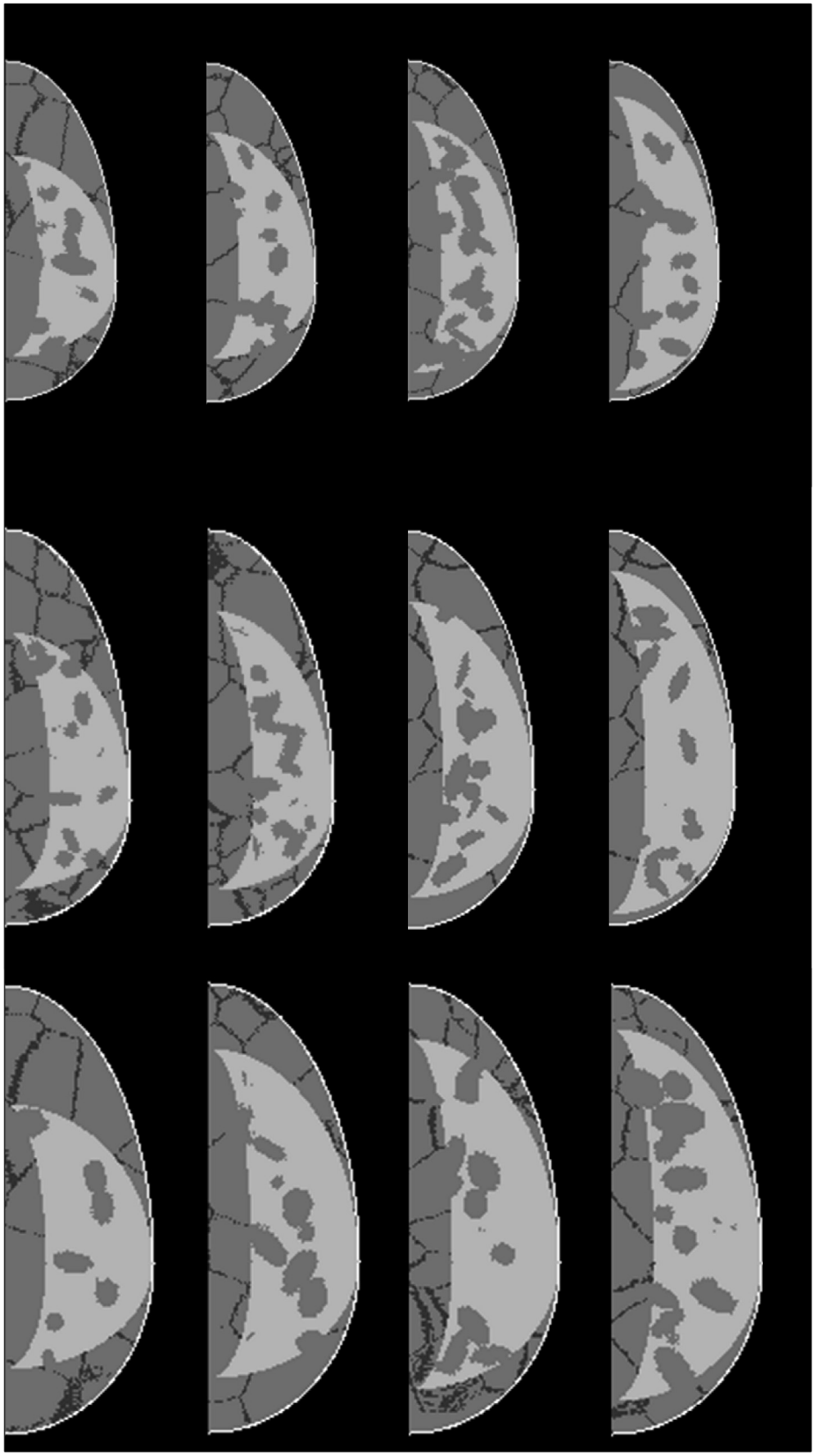

Fig. 3. Sagittal views of the ASBPs. Top to bottom: volumes 500, 750, and 1000 ml; left to right: glandularities 20%, 30%, 40%, and 50%.

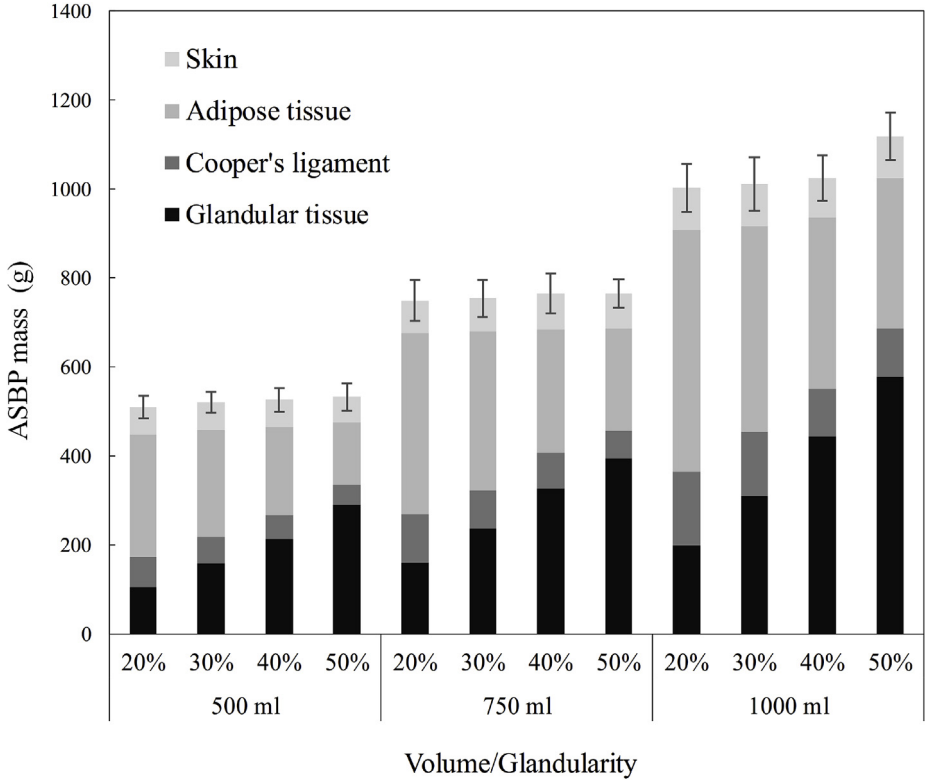

Fig. 4. Proportion of the adipose tissue, glandular tissue, Cooper's ligament, and skin in the ASBPs with various volumes and glandularities.

3. Results

3.1. Construction of ASBPs

The central sagittal views of the 500, 750, and 1000-ml ASBPs with 20%–50% glandularities are shown in Fig. 3. The grayscale intensities from dark to light represent the Cooper's ligament, adipose tissue, glandular tissue, and skin. From visual observation, the Cooper's ligaments and adipose spheres were randomly distributed in the ASBPs. Fig. 4 shows the proportion of each component in the ASBPs. The average breast masses of the 500, 750, and 1000-ml ASBPs were 521.6 ± 9.5, 757.8 ± 7.9, and 1039 ± 53.7 g. When the glandularity increased, the volumes of adipose tissue and Copper's ligament decreased correspondingly. All the ASBPs were built correctly and met the specified glandularity within 2%.

3.2. Verification of ASBPs

Fig. 5 shows the 2D projected images of the 500, 750, and 1000-ml ASBPs with 20%–50% glandularities in the mediolateral view. The glandular tissue, adipose tissue, ligament, and skin can be discerned. The higher linear attenuation coefficient of the glandular tissue resulted in the fibroglandular growth region in the projected images being brighter. The image quality of the projected ASBPs was visually evaluated by a three-year experienced clinical radiologist, who commented that images are fairly realistic in breast tissue distributions.

Table 1 shows the FD analysis results for the ASBPs with various volumes and glandularities. The ranges of the FD value for 500, 750, and 1000-ml ASBPs were 2.190–2.256, 2.193–2.261, and 2.198–2.266, respectively. The FD value slightly increased with an increase in breast volume. In addition, the FD value decreased with an increase in the proportion of glandular tissue. A possible reason is that fewer adipose ellipsoids in the fibroglandular growth region result in more uniform texture in the projected image of the ASBPs. The mean FD value for the ASBPs was 2.23, which is close to the value of 2.29 calculated using clinical mammograms (Caldwell et al., 1990). This means that the texture of the simulated breast projections matches that of the actual mammograms in terms of FD.

3.3. Breast self S values

Table 2 compares the breast self S values obtained using the ASBPs and the results calculated using OLINDA/EXM. The %CV coefficient of variation (CV) of the simulated S values was less than 1%. The S values decreased with an increase in breast volume and glandularity. For ^{18}F, the percent differences caused by different glandularities for the 500, 750, and 1000-ml ASBPs were 1.9%, 3.0%, and 3.5%, respectively. The maximum difference between the S values of the ASBPs and OLINDA/EXM was −14.4% at 500 ml/50%. For ^{99m}Tc, the minimum and maximum percent differences between the S values of the ASBPs and OLINDA/EXM occurred at 750 ml/20% and 500 ml/50%, respectively, which reached −12.1% and −16.7%. The reason for the approximately 15% lower S values of ASBPs compared with those of OLINDA/EXM is that the adipose tissue in ASBPs has a relatively lower attenuation coefficient for gamma ray, whereas the nodule module of OLINDA/EXM contains only soft tissue with a relatively higher attenuation coefficient. A material with a low attenuation coefficient attenuates less photons, resulting in less photon energy deposition and further decreasing the absorption fraction φ in equation (2). Other influencing factors include uneven distribution of the glandular tissue and the shape of the breast.

3.4. Suborgan S values

Table 3 lists the suborgan S values of target tissue caused by the distribution of ^{18}F and ^{99m}Tc in source tissue. These S values include breast as source tissue and gland as target tissue S(g←b), gland as both source and target tissues S(g←g), and gland as source tissue and mammary duct as target tissue S(d←g). The CV of the simulated results was less than 5%. The suborgan S values decreased with an increase in breast volume and glandularity. The S(g←g) had the largest value

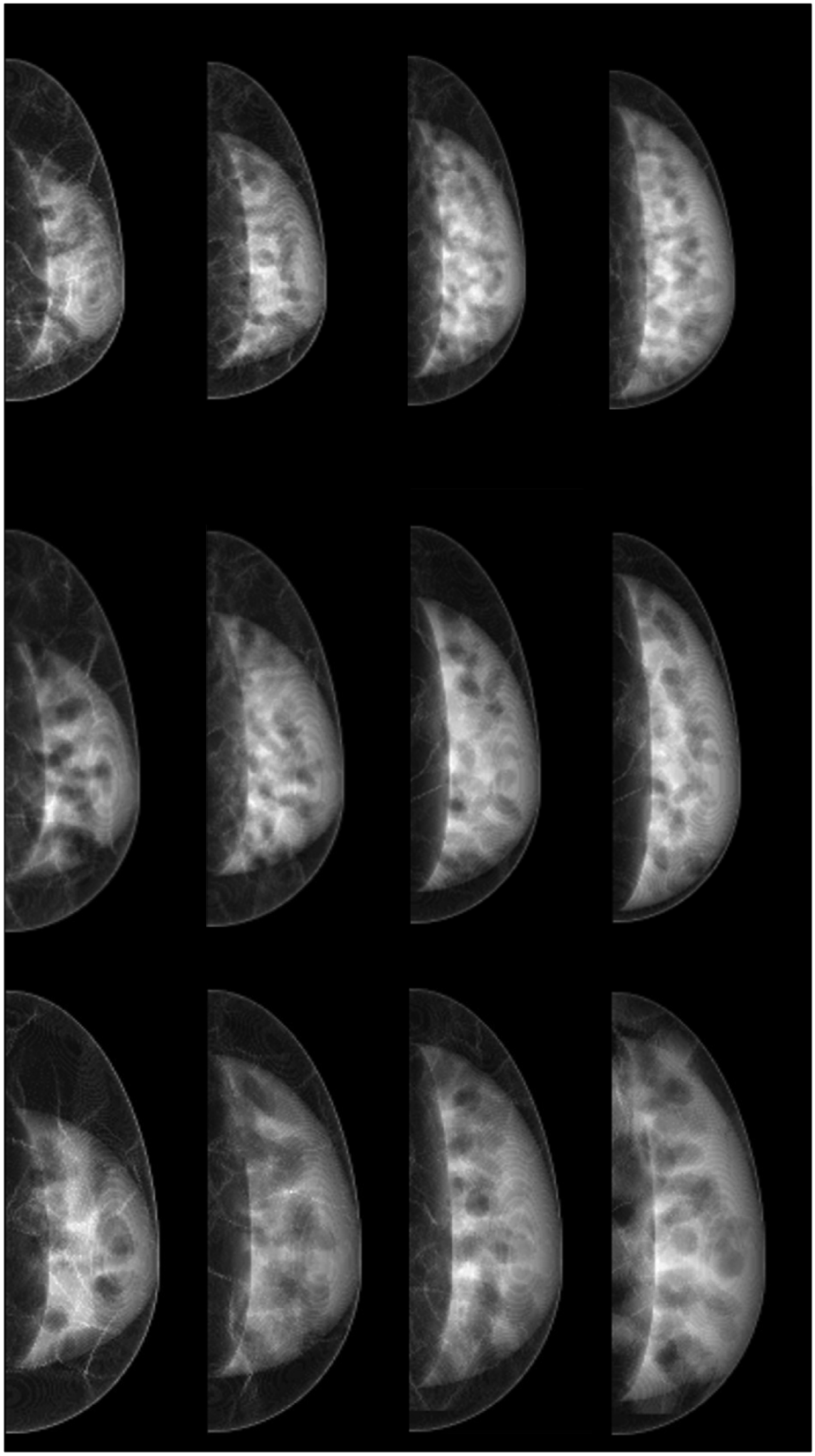

Fig. 5. Mediolateral projected images of the ASBPs. Top to bottom: volumes 500, 750, and 1000 ml; left to right: glandularities 20%, 30%, 40%, and 50%.

among the three types of suborgan S values. The main reason is that the self-absorbed fraction of charged particles is close to unity when the source and target tissues are the same. With ^{18}F as the radionuclide, S (g←g) was larger than S(b←b) with the ratios from 1.81 to 4.84. This indicates that the breast dose estimated by using the breast self S values significantly underestimates the glandular dose. The mean ratio of S (d←g) to S(g←g) was 0.296, which means that the dose of mammary ducts is approximately one-third of the dose of mammary glands.

Table 1
Mean and standard deviation of FD for the ASBPs with various volumes and glandularities.

Glandularity/Volume	500 ml	750 ml	1000 ml
20%	2.256 ± 0.029	2.261 ± 0.025	2.266 ± 0.051
30%	2.243 ± 0.018	2.246 ± 0.038	2.245 ± 0.012
40%	2.234 ± 0.031	2.232 ± 0.016	2.237 ± 0.025
50%	2.190 ± 0.036	2.193 ± 0.016	2.198 ± 0.033

Table 2
Comparison between the breast self S values S(b←b) obtained using the ASBPs and those calculated using OLINDA/EXM in the unit of mGy/MBq × s.

Isotope	Volume (ml)	OLINDA /EXM	ASBP glandularity			
			20%	30%	40%	50%
^{18}F	500	1.18E-04	1.03E-04	1.02E-04	1.01E-04	1.01E-04
	750	8.09E-05	7.31E-05	7.23E-05	7.13E-05	7.09E-05
	1000	6.32E-05	5.69E-05	5.62E-05	5.59E-05	5.49E-05
^{99m}Tc	500	9.54E-06	8.23E-06	8.08E-06	8.01E-06	7.95E-06
	750	6.74E-06	5.93E-06	5.86E-06	5.80E-06	5.75E-06
	1000	5.30E-06	4.64E-06	4.62E-06	4.54E-06	4.51E-06

Therefore, the internal dose to mammary ducts should be independently considered while evaluating the risk of ductal carcinoma.

When ^{99m}Tc was used as the source term, the ratios between S(g←g) and S(b←b) ranged from 1.74 to 3.60. As the glandularity decreased, the ratio significantly increased. For the internal dose to mammary ducts, the mean ratio of S(d←g) to S(g←g) was 0.356. Although the trend in the suborgan S value caused by ^{99m}Tc was similar to that caused by ^{18}F, the ratios of ^{99m}Tc to ^{18}F for S(g←b), S(g←g), and S(d←g) ranged from 0.07 to 0.11.

4. Discussion

Traditional mathematical phantoms used for internal dose evaluation of the breast usually have the characteristics of simple geometry and homogeneous tissue distribution. However, in reality, the distribution of breast tissues is not uniform, and significant differences in breast volume and glandularity are expected for different individuals. Although the glandularity only causes about 3% difference in breast self S values, the shape of the breast and the distribution of the breast tissues may cause a 15% difference (Table 2). Therefore, it is necessary to develop realistic breast phantoms to calculate the breast self S values. Besides, the realistic breast phantoms have to be available for glandular and duct dose assessments in breast nuclear medicine imaging. In this study, we constructed a series of ASBPs and simulated breast self S values and suborgan S values for various breast volumes and glandularities. The proposed S values can improve the accuracy of breast dose evaluation.

The ASBPs, consisting of glandular tissue, mammary ducts, adipose tissue, Cooper's ligaments, and skin, possess similar tissue structure to real breasts. The random distribution of the glandular tissue and adipose tissue can be observed in the projected images of the ASBPs. In texture analysis, FD is frequently used as a quantitative indicator for breast parenchymal pattern assessment (Verma et al., 2018). The FD values of the ASPBs are close to those calculated using clinical mammograms (Caldwell et al., 1990). These outcomes indicate that the ASBPs can represent real breasts.

As shown in Table 3, the suborgan S value decreases with an increase in the volume of ASBPs. The main reason is that the S value is defined as the product of the energy emission per disintegration from source tissue and the specific absorbed fraction of target tissue (equation (2)). In the suborgan scale from several millimeter to centimeter, the change in the absorbed fraction of photons and electrons for high-energy gamma ray in soft tissue can be neglected. An increase in the volume of ASBPs at the fixed glandularity leads to an increase in the glandular mass, which decreases the specific absorbed fraction and further the S value. In addition, as shown in Table 3, the glandularity has a significant effect on the breast suborgan S value of approximately 50%, whereas it has only 3% impact on the breast self S value as shown in Table 2.

The decay characteristic of radiation sources is another factor affecting the S value. The transformation of ^{18}F and ^{99m}Tc produces 249.8-keV positrons and 1.6-keV conversion electrons, respectively. The kinetic energy of the charged particles is almost directly deposited in the source tissue and contributes to the absorbed dose. For photon emission, the decay of ^{18}F and ^{99m}Tc produces 511-keV and 140-keV gamma rays. Since the mean free path of high energy photons in soft tissue is longer than several centimeters, the two emitted gamma rays deposit less energy within the glandular tissue. Overall, the suborgan S values of ^{18}F are higher than those of ^{99m}Tc because of energy deposition of the charged particles.

Khamwan et al. (2010) showed that the absorbed dose to the breast from ^{18}F-FDG positron emission tomography (PET) was approximately 2.287 mGy. However, the factor associated with breast cancer is the

Table 3
Suborgan S values (mGy/MBq × s) from source tissue to target tissue for the ASBPs with various volumes and glandularities.

Isotope	Volume (ml)	S value (target←source)	ASBP glandularity			
			20%	30%	40%	50%
^{18}F	500	S(g←b)	9.88E-05	8.28E-05	6.95E-05	4.96E-05
	500	S(g←g)	3.89E-04	2.77E-04	2.17E-04	1.81E-04
	500	S(d←g)	1.01E-04	7.46E-05	6.14E-05	5.29E-05
	750	S(g←b)	8.33E-05	6.47E-05	5.30E-05	4.63E-05
	750	S(g←g)	2.78E-04	2.05E-04	1.54E-04	1.27E-04
	750	S(d←g)	7.46E-05	5.83E-05	4.98E-05	4.34E-05
	1000	S(g←b)	7.13E-05	5.04E-05	4.18E-05	3.70E-05
	1000	S(g←g)	2.21E-04	1.53E-04	1.20E-04	9.93E-05
	1000	S(d←g)	5.28E-05	4.49E-05	3.96E-05	3.67E-05
^{99m}Tc	500	S(g←b)	9.49E-06	7.33E-06	6.16E-06	5.47E-06
	500	S(g←g)	2.96E-05	2.13E-05	1.67E-05	1.40E-05
	500	S(d←g)	8.91E-06	6.70E-06	5.54E-06	4.83E-06
	750	S(g←b)	7.03E-06	5.61E-06	4.67E-06	4.13E-06
	750	S(g←g)	2.13E-05	1.60E-05	1.20E-05	1.01E-05
	750	S(d←g)	6.59E-06	5.37E-06	4.68E-06	4.09E-06
	1000	S(g←b)	5.80E-06	4.46E-06	3.73E-06	3.35E-06
	1000	S(g←g)	1.87E-05	1.21E-05	9.47E-06	7.93E-06
	1000	S(d←g)	5.54E-06	4.62E-06	3.86E-06	3.53E-06

absorbed dose to the glandular tissue and mammary ducts. The S value ratio of S(g←g) to S(b←b) ranged from 1.81 to 4.84, which means that the glandular dose may reach 11 mGy depending on the breast volume and glandularity. For the absorbed dose to mammary ducts, the mean ratio of S(d←g) to S(g←g) was 0.296, implying that the duct dose is 3.26 mGy. Other source organs in BSGI and PEM can also cause glandular and duct doses. Since both glands and ducts are distributed throughout the breast, the S value from other source organs to glands or ducts is equal to the S value from other source organs to breast (Snyder, 1978). In addition, other source organs have a distance from the breast; the cross-dose S values are only 1%–5% of the breast self S values. Therefore, we can directly use the cross-dose S values to the breast from OLINDA/EXM to calculate the absorbed dose to mammary glands and ducts from other source organs.

In addition to breast nuclear medicine imaging, contrast-enhanced digital mammography (CEDM), digital breast tomosynthesis (DBT), and breast computed tomography (BCT) also have the potential for detection of mammographically occult cancer. In CEDM, the iodine-containing contrast agent is administered into patients, and the dual-energy images of the compressed breast are taken in the craniocaudal (CC) and mediolateral oblique (MLO) views. The MGD is 1.12 mGy for the CC view and 1.07 mGy for the MLO view (Tzamicha et al., 2015). DBT is usually performed along with X-ray mammography. The MGD caused by mammography ranges from 0.23 to 7.46 mGy/view (Khoury et al., 2005), whereas the patient data show the clinical glandular dose from DBT between 1.50 and 4.64 mGy (Bouwman et al., 2015). BCT is a computed tomography system dedicated to volumetric breast imaging; the phantom study shows that the MGD is between 5.6 and 17.5 mGy (Sechopoulos et al., 2010). In BSGI, an injection of 1100-MBq ^{99m}Tc-sestamibi causes approximately 2-mGy absorbed dose to the breast (Hendrick, 2010). According to the S value ratio of S(g←g) to S(b←b) proposed in this study, the glandular dose can reach 7.2 mGy, which is comparability to the MDG of other imaging modalities. However, other organs also receive a significant absorbed dose in breast nuclear medicine imaging. Therefore, it is crucial to estimate the radiation-induced cancer incidence and mortality from BSGI and PEM while considering the breast cancer deaths prevented by detection of mammographically occult cancer.

The average absorbed dose to the breast is frequently used as an indicator for breast cancer risk assessment (Hendrick, 2010; Health risks from exposur, 2006; The, 2007 recommendations, 2007). However, the administered radiopharmaceuticals in BSGI and PEM mainly accumulate in the glandular tissue. Using the average breast dose could significantly underestimate the glandular dose, meaning that we potentially underestimate the incidence of radiation-induced secondary breast cancer caused by breast nuclear medicine imaging. In addition, mammary ducts are also sensitive to radiation. Invasive ductal carcinoma is the most common type of malignancy in breasts. It accounts for more than 40% of all invasive mammary carcinomas (Makki, 2015). The proposed breast suborgan dosimetry can be used for clinical dose assessment of mammary ducts and risk evaluation of ductal carcinoma.

5. Conclusion

Proper use of breast nuclear medicine imaging as a screening method and a supplement to X-ray mammography for dense breasts can increase the detection of mammographically occult cancer. However, radiation doses to mammary glands and ducts become an issue of concern because of the high radiation sensitivity of glandular tissue. In this study, we built a series of ASBPs with various volumes and glandularities. The structure and texture of the ASBPs were verified by using the 2D projection and FD analysis. The breast self S values and suborgan S values were simulated for ^{18}F and ^{99m}Tc. The resultant suborgan S values can be used for internal dose evaluation and carcinogenic risk assessment of mammary glands and ducts in BSGI and PEM.

Conflicts of interest

The authors have declared that no competing interests exist.

Acknowledgments

This study was financially supported by grant from the Cheng Hsin General Hospital (CY10801).

References

Bakic, P.R., Albert, M., Brzakovic, D., Maidment, A.D., 2003. Mammogram synthesis using a three-dimensional simulation. III. Modeling and evaluation of the breast ductal network. Med. Phys. 30 (7), 1914–1925.
Bakic, P.R., Zhang, C., Maidment, A.D., 2011. Development and characterization of an anthropomorphic breast software phantom based upon region-growing algorithm. Med. Phys. 38 (6), 3165–3176.
Berger, M.J., 1999. XCOM: Photon Cross Section Database. http://physicsnistgov/xcom, version 1.2.
Bolch, W.E., Eckerman, K.F., Sgouros, G., Thomas, S.R., 2009. MIRD pamphlet No. 21: a generalized schema for radiopharmaceutical dosimetry–standardization of nomenclature. J. Nucl. Med. 50 (3), 477–484.
Bouchet, L.G., Bolch, W.E., Weber, D.A., Atkins, H.L., Poston, J.W., Sr, 1999. MIRD pamphlet No. 15: radionuclide S values in a revised dosimetric model of the adult head and brain. Medical Internal Radiation Dose. J. Nucl. Med. 40 (3), 62s–101s.
Bouchet, L.G., Bolch, W.E., Blanco, H.P., Wessels, B.W., Siegel, J.A., Rajon, D.A., et al., 2003. MIRD Pamphlet No 19: absorbed fractions and radionuclide S values for six age-dependent multiregion models of the kidney. J. Nucl. Med. 44 (7), 1113–1147.
Bouwman, R.W., van Engen, R.E., Young, K.C., den Heeten, G.J., Broeders, M.J., Schopphoven, S., et al., 2015. Average glandular dose in digital mammography and digital breast tomosynthesis: comparison of phantom and patient data. Phys. Med. Biol. 60 (20), 7893–7907.
Caldwell, C.B., Stapleton, S.J., Holdsworth, D.W., Jong, R.A., Weiser, W.J., Cooke, G., et al., 1990. Characterisation of mammographic parenchymal pattern by fractal dimension. Phys. Med. Biol. 35 (2), 235–247.
Chen, B., Shorey, J., Saunders Jr., R.S., Richard, S., Thompson, J., Nolte, L.W., et al., 2011. An anthropomorphic breast model for breast imaging simulation and optimization. Acad. Radiol. 18 (5), 536–546.
Coffey, J.L., Cristy, M., Warner, G.G., 1981. Specific absorbed fractions for photon sources uniformly distributed in the heart chambers and heart wall of a heterogeneous phantom. J. Nucl. Med. 22 (1), 65–71.
Drooger, J.C., Hooning, M.J., Seynaeve, C.M., Baaijens, M.H., Obdeijn, I.M., Sleijfer, S., et al., 2015. Diagnostic and therapeutic ionizing radiation and the risk of a first and second primary breast cancer, with special attention for BRCA1 and BRCA2 mutation carriers: a critical review of the literature. Cancer Treat Rev. 41 (2), 187–196.
Erickson, D.W., Wells, J.R., Sturgeon, G.M., Samei, E., Dobbins 3rd, J.T., Segars, W.P., et al., 2016. Population of 224 realistic human subject-based computational breast phantoms. Med. Phys. 43 (1), 23.
Going, J.J., Moffat, D.F., 2004. Escaping from Flatland: clinical and biological aspects of human mammary duct anatomy in three dimensions. J. Pathol. 203 (1), 538–544.
Hammerstein, G.R., Miller, D.W., White, D.R., Masterson, M.E., Woodard, H.Q., Laughlin, J.S., 1979. Absorbed radiation dose in mammography. Radiology 130 (2), 485–491.
Health Risks from Exposure to Low Levels of Ionizing Radiation: BEIR VII Phase 2. National Academies Press.
Hendrick, R.E., 2010. Radiation doses and cancer risks from breast imaging studies. Radiology 257 (1), 246–253.
Hernandez, A.M., Seibert, J.A., Boone, J.M., 2015. Breast dose in mammography is about 30% lower when realistic heterogeneous glandular distributions are considered. Med. Phys. 42 (11), 6337–6348.
Hofvind, S., Geller, B.M., Skelly, J., Vacek, P.M., 2012. Sensitivity and specificity of mammographic screening as practised in Vermont and Norway. Br. J. Radiol. 85 (1020), e1226–1232.
Hruska, C.B., 2017. Molecular breast imaging for screening in dense breasts: state of the art and future directions. AJR Am. J. Roentgenol. 208 (2), 275–283.
Khamwan, K., Krisanachinda, A., Pasawang, P., 2010. The determination of patient dose from (18)F-FDG PET/CT examination. Radiat. Prot. Dosim. 141 (1), 50–55.
Khoury, H.J., Barros, V.S., Lopes, C., 2005. Evaluation of patient dose for mammography in Pernambuco, Brazil. Radiat. Prot. Dosim. 115 (1–4), 337–339.
Lai, C.J., Zhong, Y., Yi, Y., Wang, T., Shaw, C.C., 2015. Radiation doses in volume-of-interest breast computed tomography–A Monte Carlo simulation study. Med. Phys. 42 (6), 3063–3075.
Lazos, D., Kolitsi, Z., Pallikarakis, N., 2000. A software data generator for radiographic imaging investigations. IEEE Trans. Inf. Technol. Biomed. 4 (1), 76–79.
Loevinger, R., Budinger, T.F., Watson, E.E., 1988. MIRD Primer for Absorbed Dose Calculations. Society of Nuclear Medicine.
Mahr, D.M., Bhargava, R., Insana, M.F., 2012. Three-dimensional in silico breast phantoms for multimodal image simulations. IEEE Trans. Med. Imaging 31 (3), 689–697.
Makki, J., 2015. Diversity of breast carcinoma: histological subtypes and clinical relevance. Clin. Med. Insights Pathol. 8, 23–31.
Mohammadyari, P., Faghihi, R., Mosleh-Shirazi, M.A., Lotfi, M., Hematiyan, M.R., Koontz, C., et al., 2015. Calculation of dose distribution in compressible breast tissues using finite element modeling, Monte Carlo simulation and thermoluminescence

dosimeters. Phys. Med. Biol. 60 (23), 9185–9202.
Nigapruke, K., Puwanich, P., Phaisangittisakul, N., Youngdee, W., 2010. Monte Carlo simulation of average glandular dose and an investigation of influencing factors. J. Radiat. Res. 51 (4), 441–448.
Ohtake, T., Kimijima, I., Fukushima, T., Yasuda, M., Sekikawa, K., Takenoshita, S., et al., 2001. Computer-assisted complete three-dimensional reconstruction of the mammary ductal/lobular systems: implications of ductal anastomoses for breast-conserving surgery. Cancer 91 (12), 2263–2272.
Pelowitz, D.B., Durkee, J.W., Elson, J.S., Fensin, M.L., Hendricks, J.S., James, M.R., et al., 2011. MCNPX 2.7E Extensions. Los Alamos National Lab.
Sarno, A., Dance, D.R., van Engen, R.E., Young, K.C., Russo, P., Di Lillo, F., et al., 2017. A Monte Carlo model for mean glandular dose evaluation in spot compression mammography. Med. Phys. 44 (7), 3848–3860.
Sechopoulos, I., Feng, S.S., D'Orsi, C.J., 2010. Dosimetric characterization of a dedicated breast computed tomography clinical prototype. Med. Phys. 37 (8), 4110–4120.
Snyder, W., 1978. Estimates of specific absorbed fractions for monoenergetic photon sources uniformly distributed in various organs of a heterogeneous phantom. MIRD pamphlet 5.
Stabin, M.G., Sparks, R.B., Crowe, E., 2005. OLINDA/EXM: the second-generation personal computer software for internal dose assessment in nuclear medicine. J. Nucl. Med. 46 (6), 1023–1027.
The 2007 recommendations of the international commission on radiological protection. ICRP publication 103. Ann. ICRP 37 (2–4), 1–332.
Tourassi, G.D., Delong, D.M., Floyd Jr., C.E., 2006. A study on the computerized fractal analysis of architectural distortion in screening mammograms. Phys. Med. Biol. 51 (5), 1299–1312.
Tzamicha, E., Yakoumakis, E., Tsalafoutas, I.A., Dimitriadis, A., Georgiou, E., Tsapaki, V., et al., 2015. Dual-energy contrast-enhanced digital mammography: glandular dose estimation using a Monte Carlo code and voxel phantom. Phys. Med. 31 (7), 785–791.
Verma, G., Luciani, M.L., Palombo, A., Metaxa, L., Panzironi, G., Pediconi, F., et al., 2018. Microcalcification morphological descriptors and parenchyma fractal dimension hierarchically interact in breast cancer: a diagnostic perspective. Comput. Biol. Med. 93, 1–6.
Villoing, D., Lee, A.K., Choi, H.D., Lee, C., 2019. S values for neuroimaging procedures on Korean pediatric and adult head computational phantoms. Radiat. Prot. Dosim. https://doi.org/10.1093/rpd/ncy1287.